Dalton Transactions

ROYAL SOCIETY OF CHEMISTRY

PAPER

View Article Online
View Journal | View Issue

Cite this: *Dalton Trans.*, 2025, **54**, 5764

High temperature interactions of lead palmitate with linseed oil†

Ruslan Barannikov, [a,b] Joen Hermans, [c,d,e] Jiří Plocek,[a] Petr Bezdička,[a] Anna Vykydalová,[a] Andrii Mahun,[f] Libor Kobera [f] and Silvie Švarcová *[a]

Received 22nd November 2024,
Accepted 4th March 2025

DOI: 10.1039/d4dt03267e

rsc.li/dalton

This study investigates the high-temperature interactions between lead palmitate ($Pb(C16)_2$) and linseed oil, revealing complex phase transformations and structural changes critical for understanding metal soap formation in oil paintings. Through complementary analytical techniques including DSC, XRPD, FTIR, and solid-state NMR, we identified two significant phenomena: the formation of mixed lead palmitate–stearate compounds and the emergence of a high-temperature lead palmitate polymorph. When heated to 112 °C, lead palmitate in linseed oil undergoes partial conversion to mixed lead palmitate–stearate complexes, likely due to interactions with stearic acid present in the oil either in a free form or as a part of triglycerides. Additionally, we observed the formation of a metastable high-temperature polymorph characterized by hemi-directed coordination around lead atoms, similar to structures found in short-chain lead carboxylates. The transformation kinetics of this polymorph appears as a complex process influenced by several factors. These findings provide crucial insights into the behavior of lead soaps in oil paintings during thermal treatments and contribute to our understanding of metal soap-induced degradation in artistic and cultural heritage materials.

1. Introduction

Metal soaps are a class of metal carboxylates formed by the reaction between metal ions and saturated fatty acids. These versatile materials find diverse applications across various industries due to their unique properties. For example, they serve as surfactants and dispersing agents,[1,2] antibacterial agents,[3] plasticizers in ionomeric polymers[4] and precursors in the synthesis of nanoparticles and nanocomposites.[5,6]

In recent years, metal carboxylates have gained particular importance in conservation science, especially in the context of oil paintings. These compounds form within painting layers as a result of interactions between different metal-based pigments and fatty binders such as drying oils or egg yolk. Lead soaps, especially those of palmitic or stearic acids, attracted significant attention in conservation research due to their prevalence in historical oil paintings and their role in causing structural changes and degradation in artworks over time.[7–11] The literature also documents that artists and paint manufacturers added fatty acid salts and lead driers to paints to accelerate the drying of paint layers.[12,13] Additionally, various metal soaps, including lead soaps, were mixed with pigments to aid the milling process.[14,15] Both of these practices may pose further risks to the long-term preservation of oil paintings.

Understanding the thermal properties of lead soaps, whether present as a result of degradation or added as driers, is crucial for determining safe methods of display, cleaning, and restoration of valuable pieces of artworks. This knowledge is particularly important in the context of conservation techniques that utilize high-temperature treatments, such as relining. Relining is a technique applied to degraded artwork canvases to reinforce them by ironing a new canvas on the reverse side of the painting, utilizing various adhesives based on wax, resins, glue or acrylates. This process can cause irreversible changes in the artwork's stability and appearance.[16–18]

[a]*Institute of Inorganic Chemistry of the Czech Academy of Sciences, Husinec 1001, 250 68 Husinec-Řež, Czech Republic. E-mail: svarcova@iic.cas.cz, barannikov@iic.cas.cz, plocek@iic.cas.cz, bezdicka@iic.cas.cz, vykydalova@iic.cas.cz; Tel: +420 311 236 946*
[b]*Department of Inorganic Chemistry, Faculty of Science, Charles University in Prague, Hlavova 2030/8, 128 40 Prague, Czech Republic*
[c]*Van't Hoff Institute for Molecular Sciences, University of Amsterdam, PO Box 94157, 1090GD Amsterdam, The Netherlands. E-mail: j.j.hermans@uva.nl*
[d]*Conservation & Restoration, Amsterdam School of Heritage, Memory and Material Culture, University of Amsterdam, PO Box 94552, 1090GN Amsterdam, The Netherlands*
[e]*Conservation & Science, Rijksmuseum, Hobbemastraat 22, 1071ZC Amsterdam, The Netherlands*
[f]*Institute of Macromolecular Chemistry of the Czech Academy of Sciences, Heyrovskeho nam. 2, 162 00 Prague 6, Czech Republic. E-mail: mahun@imc.cas.cz, kobera@imc.cas.cz*

† Electronic supplementary information (ESI) available. See DOI: https://doi.org/10.1039/d4dt03267e

Numerous research papers have reported on lead carboxylates, revealing their crystal structure[19–30] thermal behavior[20,31–34] and crystallization kinetics.[35] Particular attention is paid to the lead palmitate ($Pb(C16)_2$) and lead stearate ($Pb(C18)_2$) as they are often found in degraded areas of paintings.

It is known that $Pb(C16)_2$ and $Pb(C18)_2$ exhibit polymorphism, going through an intermediate (rotator) solid phase (SI) before melting.[20,21,31,32] However, this stepwise transition process has been reported to be affected by the presence of linseed oil, as revealed during a study of mixtures of synthesized lead palmitate and linseed oil.[32] During the crystallization of lead palmitate in linseed oil from the melt, a possible reaction between them may occur, resulting in the formation of additional lead carboxylate phases.[32] Several studies have documented the formation of unknown lead carboxylates resulting from the interaction of lead-based pigments with linseed oil at elevated temperatures.[36–39]

Our research builds upon previous works, investigating not only the thermal behavior of lead palmitate in linseed oil, but also the complex crystallization processes that occur in polymerized oil binders. While this study uses fresh linseed oil rather than aged oil matrices found in historical paintings, our findings provide valuable insights into the fundamental behavior of lead soaps within constraining oil environments. Although historical paint samples contain higher concentrations of polar functional groups and different levels of cross-linking that may affect lead soap solubility and crystallization kinetics, understanding these interactions in a simpler system is crucial for interpreting the unusual structures and disorder levels observed in paint samples.

Through a multi-analytical approach combining differential scanning calorimetry (DSC), temperature-dependent attenuated total reflection Fourier transform infrared spectroscopy (ATR-FTIR), *in situ* high-temperature X-ray powder diffraction (*in situ* HT-XRPD), and solid-state nuclear magnetic resonance (ssNMR), we studied lead palmitate formation and transformation in linseed oil medium. This comprehensive analysis aims to elucidate both temperature-induced changes and crystallization processes, addressing the recently detected unidentified lead carboxylates observed in model samples and authentical paint samples.[36–39] By examining lead soap behavior during thermal cycling in oil-rich environments, our research provides insights into the formation mechanisms and potential mesophases that may occur in polymerized oil binders, contributing to a broader understanding of lead soap dynamics in historical paintings.

2. Experimental

2.1. Materials and experiments

Lead palmitate ($Pb(C16)_2$, where C16 stands for $C_{15}H_{31}COO^-$) was synthesized in the form of powder by the precipitation procedure *via* triethylamine salts of palmitic acid as previously described in detail elsewhere.[30] The reaction used a 2 : 1 stoichiometric ratio of palmitic acid to lead acetate. Lead octanoate ($Pb(C8)_2$, where C8 stands for $C_7H_{15}COO^-$) and lead stearate ($Pb(C18)_2$, where C18 stands for $C_{17}H_{35}COO^-$) were synthesized using the same procedure.

Table 1 provides an overview of examined samples, their identification codes, brief description of their treatment, and the corresponding analytical methods applied to each sample. The preparation of mixtures containing $Pb(C16)_2$ and linseed oil (LO) was carried out using fresh (*i.e.*, unpolymerized) cold-pressed linseed oil (Kremer Pigmente) with a low acid content. The oil was used as received, without pre-polymerization, to study the interactions between lead palmitate and the polymerizing oil medium – a scenario that allows us to observe the full range of potential interactions during the polymerization process. The mixtures were prepared using a fixed mass ratio of 1 : 3 ($Pb(C16)_2$ + LO_mix), corresponding to a molar fraction of approximately 0.289 $Pb(C16)_2$ in the mixture, based on the molar masses of $Pb(C16)_2$ (718 g mol^{-1}) and LO (875 g mol^{-1}). Specifically, 50 mg of synthesized $Pb(C16)_2$ was mixed with 150 mg of LO and thoroughly homogenized using a mortar and pestle. Multiple analytical techniques employed throughout this study including FTIR, GC-FID and ssNMR confirmed the initial unpolymerized state of the oil and enabled comprehensive characterization of its subsequent transformations.

For the high-temperature experiments, the mixture of $Pb(C16)_2$ and LO, was uniformly applied to a copper disk (20 mm diameter, 0.2 mm thickness) creating a film approximately 0.5–0.7 mm thick. Copper was chosen for its superior thermal

Table 1 Sample descriptions and applied analytical methods

Code	Sample description	Applied methods[a]
$Pb(C16)_2$	Pure powder palmitate $Pb(C_{15}H_{31}COO)_2$	HT-ATR-FTIR, *in situ* HT-XRPD, DSC
$Pb(C18)_2$	Pure powder stearate $Pb(C_{17}H_{35}COO)_2$	DSC
$Pb(C16)_2$ + LO_mix	$Pb(C16)_2$ and LO mixture	ATR-FTIR, XRPD, *in situ* HT-XRPD, DSC
$Pb(C16)_2$ + LO_112 °C	$Pb(C16)_2$ and LO mixture isothermally heated at 112 °C for 2 hours and rapidly cooled down in N_2(l)	ATR-FTIR, trans-FTIR, XRPD, ssNMR
$Pb(C8)_2$	Pure powder octanoate $Pb(C_7H_{15}COO)_2$	ATR-FTIR
LO	Linseed oil	HR-NMR

[a] ATR-FTIR – attenuated total reflection Fourier transformed infrared spectroscopy, HT-ATR-FTIR – temperature dependent ATR-FTIR, trans-FTIR – transmission FTIR, XRPD – X-ray powder diffraction, *in situ* HT-XRPD – *in situ* high-temperature XRPD, ssNMR – solid-state nuclear magnetic resonance, HR-NMR – high-resolution NMR, DSC – differential scanning calorimetry.

conductivity, ensuring efficient heat transfer to the sample. The heating setup consisted of a laboratory stirrer with a heating plate, which was shielded by a duralumin plate to promote uniform heat distribution and increase heat capacity (Fig. S1, ESI†). The coated copper disk was heated at 112 °C for two hours. To maintain stable temperature conditions, the sample was covered with aluminum foil and insulated with alumina wool. The temperature was regulated by the stirrer's external sensor and monitored by calibrated system K-thermocouple (T300) + datalogger (Greisinger GMH 3200). Both sensors were positioned in close thermal contact with the duralumin plate near the sample. Following the two-hour heating period, the sample ($Pb(C16)_2$ + LO_112 °C) was rapidly quenched in liquid nitrogen for 10–15 minutes and analyzed immediately after removing the sample from the liquid nitrogen.

The temperature of 112 °C was selected based on our preliminary DSC and HT-XRPD analyses, which indicated significant phase transformations at this temperature point. While this temperature exceeds typical conservation treatment temperatures[16–18] it was chosen to enable comprehensive characterization of the transformation products under conditions where the reactions proceed to completion within a reasonable timeframe. This approach provides a fundamental understanding of potential transformation pathways that may occur more slowly at the lower temperatures used in conservation practice.

2.2. Fourier transform infrared spectroscopy (FTIR)

ATR-FTIR spectra of $Pb(C16)_2$ + LO_mix, $Pb(C16)_2$ + LO_112 °C and $Pb(C8)_2$ were recorded using the Nicolet Nexus 670 FTIR spectrometer equipped with a diamond crystal for attenuated total reflection (ATR). The spectra were recorded in a range of 4000–400 cm^{-1} with a resolution of 4 cm^{-1}, number of scans 64. Spectra were not baseline corrected. Qualitative evaluation of acquired data was performed with the Thermo Scientific OMNIC 9 v9.2.86 software for optical and/or vibrational spectroscopy.

Long-term trans-FTIR measurements of $Pb(C16)_2$ + LO_112 °C were performed in a transmission mode using the Vertex V70 (Bruker Optics, Germany) spectrometer with resolution of 4 cm^{-1} and accumulation of 64 scans, in a range from 4000 to 400 cm^{-1}. For regular measurements performed every 24 hours the sample was applied using a palette knife on a monocrystalline silicon disk transparent to IR radiation and stored under stable ambient conditions during the whole experiment with monitored temperature (T) and relative humidity (RH), having an average T = 22.7 °C (±0.5 °C) and RH = 35% (±5.0%). The conditions were comparable with the storage of the sample for long-term XRPD measurements. Acquisition and qualitative evaluation of data were performed in the OPUS 8.5 spectroscopy software (Bruker Optics, Germany).

Temperature-dependent HT-ATR-FTIR spectroscopy of powder $Pb(C16)_2$ was conducted using a PerkinElmer Frontier spectrometer equipped with a heatable diamond GladiATR module from Pike Technologies. Spectra were obtained as single scans at a resolution of 1 cm^{-1} in a range from 4000 to 450 cm^{-1}. The sample was placed on the ATR crystal and gradually heated to 150 °C with 20 °C min^{-1} and then rapidly cooled using a pre-cooled brass heat sink, while 5 to 6 spectra were collected per minute. To determine the sample temperature during spectrum collection accurately, the linear relationship established between temperature and the background phonon signal of the diamond ATR crystal at 2155 cm^{-1} was employed (Fig. S2, ESI†).[35]

2.3. X-ray powder diffraction (XRPD)

Diffraction patterns of $Pb(C16)_2$ + LO_mix and $Pb(C16)_2$ + LO_112 °C were collected with a PANalytical X'PertPRO MPD diffractometer equipped with a conventional X-ray tube ($Co_{K\alpha}$ radiation, 40 kV, 30 mA, line focus) and an X'Celerator multichannel detector with an anti-scatter shield. The measurements were performed in conventional Bragg–Brentano geometry over a range of 1.5 to 50° 2θ, with a step size of 0.0167° and 200 s counting time per step, resulting in approximately 80-minute scans. The incident beam configuration included a 0.02 rad Soller slit, 1/16° divergence slit, 1/8° anti-scatter slit, and 15 mm mask, while the diffracted beam was configured with a 5.0 mm anti-scatter slit, 0.02 rad Soller slit, and Fe beta-filter. For studying phase transformation, long-term XRPD measurements of the $Pb(C16)_2$ + LO_112 °C sample were conducted over a two-week period. The sample was prepared by applying a thin layer on a zero background silicon holder using a palette knife. Measurements were taken at 12-hour intervals under controlled ambient conditions, maintaining an average temperature of 23 °C (±0.5 °C) and relative humidity of 32% (±5.0%). To ensure data consistency and minimize environmental interference, the sample remained fixed in the diffractometer sample stage throughout the entire experimental period.

High temperature diffraction patterns were collected *in situ* with a PANalytical X'PertPRO diffractometer equipped with a conventional X-ray tube ($Co_{K\alpha}$ radiation, 40 kV, 30 mA, line focus) and a multichannel detector X'Celerator with an anti-scatter shield. For experiments at elevated temperature the high temperature chamber (HTK 16, Anton Paar, Graz, Austria) was used. XRPD patterns were measured for $Pb(C16)_2$ and $Pb(C16)_2$ + LO_mix at various temperature ranges. For $Pb(C16)_2$, patterns were collected at 25 °C and between 30 °C and 130 °C, both heating and cooling. For $Pb(C16)_2$ + LO_mix, the range was 30 °C to 110 °C, also in both directions. The measurements were made in 10 °C increments within the 5° to 26° 2θ range, with a dwell of approximately 11 minutes at each temperature. *In situ* isothermal measurements for both samples were conducted also in the interval 5–26° 2θ, starting at 25 °C, then rapidly heated to 112 °C (rate *ca.* 60 °C min^{-1}), kept at this temperature for two hours and finally, cooled down (60 °C min^{-1}) to 25 °C. Qualitative analysis was performed with the HighScorePlus software package[40] (Malvern PANalytical, The Netherlands, version 4.9.0) and PDF-4+ database.[41]

The Profex 5.4.1/BGMN 4.2.23 software code was used for the estimation of mass fractions of crystalline phases and crystallite sizes of lead palmitate polymorphs. This software performs the whole profile refinement based on the Rietveld method.[42–45] The model of low temperature polymorph of lead palmitate (PDF # 02-103-9663), *catena*-(bis(μ-hexadecanoato)-lead(II)) was taken from PDF 5+ database.[41] The model of the high temperature polymorph of lead palmitate was adapted from the low temperature one. Estimated standard deviations (ESD) were calculated as implemented within the BGMN program. The ESD for mass fractions were calculated according to recommendations in the documentation of the HighScorePlus software package as ESD * GoF (goodness of fit).[46] Further details on the computing procedures are reported in ESI.†

2.4. Solid-state nuclear magnetic resonance (ssNMR)

Experimental ^{207}Pb ssNMR spectra were recorded at 16.4 T using a Bruker NEO spectrometer equipped with a 3.2 mm cross-polarization magic angle spinning (CP/MAS) probe. The spectra were recorded at the Larmor frequency of $\nu(^{207}\text{Pb})$ = 146.387 MHz. The ^{207}Pb chemical shifts were calibrated using solid $Pb(NO_3)_2$ (δ_{iso} = −3473.6 ppm) as an external standard. Experimental ^{207}Pb NMR spectra were recorded at static conditions using the WURST-CPMG[47,48] and spin-echo[49] pulse sequences. The 50 μs CT selective pulse (WURST-80) was applied with 7 s recycle delay and 4k scans. The 1 MHz WURST sweep width (LTH) and 75 loops in the CPMG echo train were used. The ^{207}Pb spikelet NMR spectrum (with 5000 Hz spike separation) was obtained at one offset position at −220 kHz. The spin-echo experiment was carried out at static conditions, the delay between pulses was 90 μs and the pulse π/2 length was set to 2.3 μs at 100 W with 7 s recycle delay and 70k scans. High-power CW ^{1}H decoupling was used to eliminate heteronuclear dipolar couplings in all measurements. The ^{207}Pb spin-echo NMR spectrum was obtained at the offset position at −120 kHz. The finely powdered samples were packed into 3.2 mm ZrO_2 rotors and stored at laboratory temperature. Temperature of 268.2 K was maintained for all NMR experiments and the temperature calibration was performed on $Pb(NO_3)_2$.[50] All ssNMR spectra were processed using Top Spin 3.5 pl7 software package.

2.5. Differential scanning calorimetry (DSC)

DSC measurements were performed on Netzsch STA449 F1 Jupiter (Netzsch, Selb, Germany) equipped with an intracooler. Samples of weight around 10 mg were measured in two parallels, placed into an open alumina crucible. Argon was used as a purge gas. The flow was 50 ml min^{-1}. Powder $Pb(C16)_2$ was heated from 40 to 140 °C at 2 °C min^{-1}, cooled down to 40 °C at 2 °C min^{-1} and again heated up to 140 °C. $Pb(C16)_2$ + LO_mix was heated from 40 to 112 °C at 2 °C min^{-1}, cooled down to 40 °C at 2 °C min^{-1} and again heated up to 112 °C. The criteria selected for determining the melting (T_m) and crystallization temperature (T_c) were based on the peak's onset. The enthalpies of melting (ΔH_m) and crystallization (ΔH_m^c) were obtained based on the sample weight using the software Proteus61.

3. Results and discussion

3.1. High temperature interactions of lead palmitate with linseed oil

3.1.1 Differential scanning calorimetry (DSC). To investigate the thermal behavior of lead palmitate in linseed oil and identify potential phase transitions, we first performed DSC analysis. During thermal analysis, powder $Pb(C16)_2$ demonstrates characteristic mesomorphic phase behavior, exhibiting stepwise melting and crystallization processes as evidenced by DSC thermograms (Fig. S3a, ESI†). In accordance with previous investigations,[19,21,24,27,30,32,33] $Pb(C16)_2$ undergoes an endothermic transition from solid crystalline phase (SII) to an intermediate (rotator) solid phase (SI) at 109.5 °C. The SI phase is characterized by a high crystallinity and rotational motion of the alkyl chains, resulting in internal orientational disorder.[19–23] Subsequently, SI converts to the isotropic liquid (IL) phase at 116.2 °C, with reversible transformations observed during the exothermic process (Table S1†).

On the other hand, the DSC heating curve of the $Pb(C16)_2$ + LO_mix sample (Fig. 1) reveals a broad endothermic signal with significantly reduced transition temperature. The SII → SI and SI → IL transitions appear to merge, with an onset temperature 98.9 °C and a maximum at 106.9 °C. The crystallization onset temperature during cooling (105 °C) is notably lower compared to the pure powder sample (Table S1†). Furthermore, the exothermic curve exhibits multiple distinct signals with maxima at 102.1 °C, 98.9 °C, 93.7 °C, and 89.8 °C indicating the formation of additional lead carboxylate phases (Table 2). Reproduced DSC measurements confirmed these observations (Fig. S4†). These findings align with the work of Hermans *et al.*,[32] who investigated metal soap crystallization in linseed oil using DSC. Their research demonstrated that interactions between lead palmitate and linseed oil molecules during crystallization are favored over lead palmitate self-interactions, particularly at lower lead palmitate concentrations (0.1–0.4 molar fraction) in linseed oil. The authors established that both the transition temperatures and the number of observable phase transformations are strongly dependent on metal soap concentration and the degree of linseed oil polymerization. For lead palmitate in linseed oil, the SII → SI and SI → IL transitions become indistinguishable, merging at approximately 0.6 and 0.3 molar fractions of $Pb(C16)_2$ during heating and cooling, respectively, consistent with our observations (Fig. 1).[32]

However, our investigation revealed additional signals during the exothermic process that were not previously reported by Hermans *et al.* (2016).[32] This discrepancy may be attributed to their higher maximum analysis temperature (130 °C), which could have obscured subtle structural rearrangements and/or phase transformations observable at lower temperatures. Our modified approach, limiting the

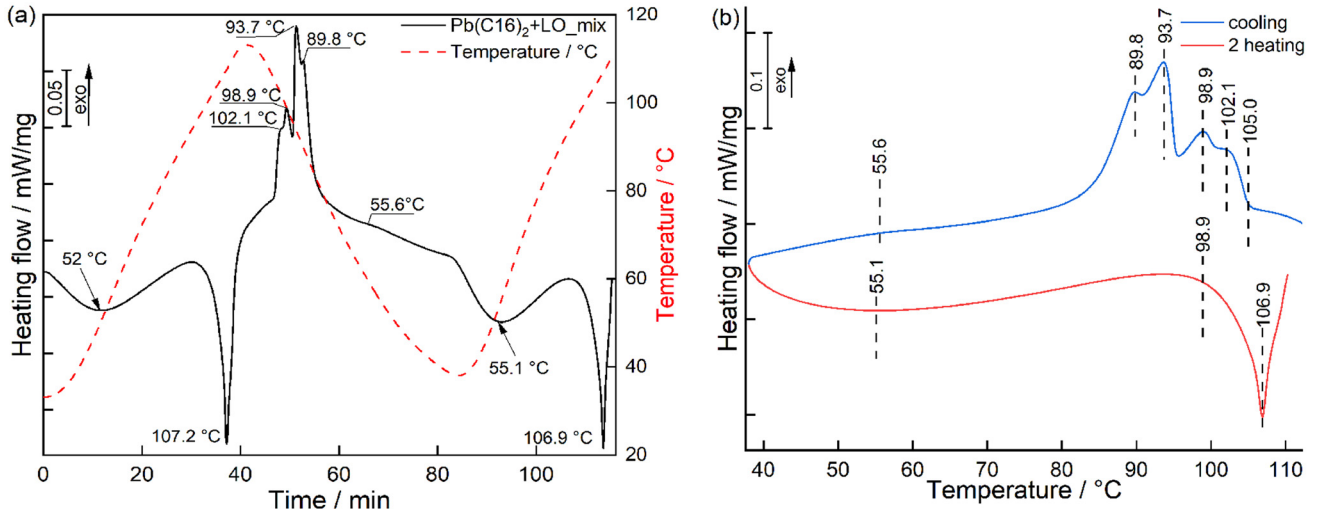

Fig. 1 DSC record of $Pb(C16)_2$ + LO_mix as a function of time (a) and temperature (b).

Table 2 Thermal properties of $Pb(C16)_2$ + LO_mix obtained from DSC data

	2nd heating			Cooling		
Sample	T_{onset}/°C	T_{max}/°C	ΔH_m/J g^{-1}	T_{onset}/°C	T_{max}/°C	ΔH_m^c/J g^{-1}
$Pb(C16)_2$ + LO_mix*	98.9	106.9	22.46	105.0	102.1; 98.9; 93.7; 89.8	−46.87

*Data for powder $Pb(C16)_2$ are provided in Table S1, ESI†.

maximum temperature to 112 °C where local order around lead atoms may persist[19,21] enabled the detection of these additional thermal events.

A significant discrepancy between melting (22.46 J g^{-1}) and crystallization (−46.87 J g^{-1}) enthalpies was observed (Table 2). The interpretation of this substantial energy difference is complicated by the system's complexity, as it contains a mixture of lead palmitate and linseed oil that may undergo continuous compositional changes during thermal treatment.

The DSC thermograms reveal a broad endothermic signal at approximately 55 °C that shows notable intensification during the second heating cycle (Fig. 1a), an observation confirmed through reproduced experiment (Fig. S4, ESI†). This broad transition suggests some interaction between the oil and Pb $(C16)_2$ or subtle loss of order in $Pb(C16)_2$ structure, but the identification of the true nature of it is challenging with just DSC.

Nevertheless, the emergence of novel DSC signals definitively confirms the formation of additional lead carboxylate phases. This observation prompted further investigation of the mixture's thermal behavior using complementary analytical techniques to elucidate the structural characteristics of these observed processes.

3.1.2 *In situ* high-temperature X-ray powder diffraction (*in situ* HT-XRPD). To characterize the structural changes associated with the thermal transitions observed by DSC and to identify potential new crystalline phases, we performed *in situ* HT-XRPD analysis of $Pb(C16)_2$ + LO_mix up to 110 °C to correlate with the DSC procedure (Fig. 1). For powder Pb $(C16)_2$, the *in situ* HT-XRPD measurement was extended to 130 °C to fully characterize its complete phase transformation sequence. This higher temperature range was necessary as pure lead palmitate exhibits a melting point of 116.2 °C (as determined by DSC), and observing the formation and subsequent recrystallization behavior of the isotropic liquid (IL) phase required heating above this temperature. In contrast, the presence of linseed oil in $Pb(C16)_2$ + LO_mix lowers the phase transition temperatures, with DSC showing merged SII → SI and SI → IL transitions beginning at 98.9 °C, making the 110 °C maximum sufficient for characterizing the formation of additional crystalline phases in this system.

Lead palmitate (SII phase) as well as lead stearate and mixed lead palmitate–stearates crystallize in the monoclinic space group *P*2/*c*. Their layered structures reflecting the arrangement of long hydrocarbon chains provide characteristic XRPD patterns. In XRPD, these long-chain carboxylates are distinguishable especially by inspection of positions of basal *h*00 diffraction lines corresponding to the change of lattice parameter *a* ranging from 90.604 Å (lead palmitate) to 100.772 Å (lead stearate).[21,30]

In the $Pb(C16)_2$ + LO_mix sample, a decrease in the *h*00 basal diffraction line intensities is observed already at 100 °C (Fig. 2a), while in powder $Pb(C16)_2$ noticeable changes are observed only at 110 °C (Fig. 2c). The observed shift of melting

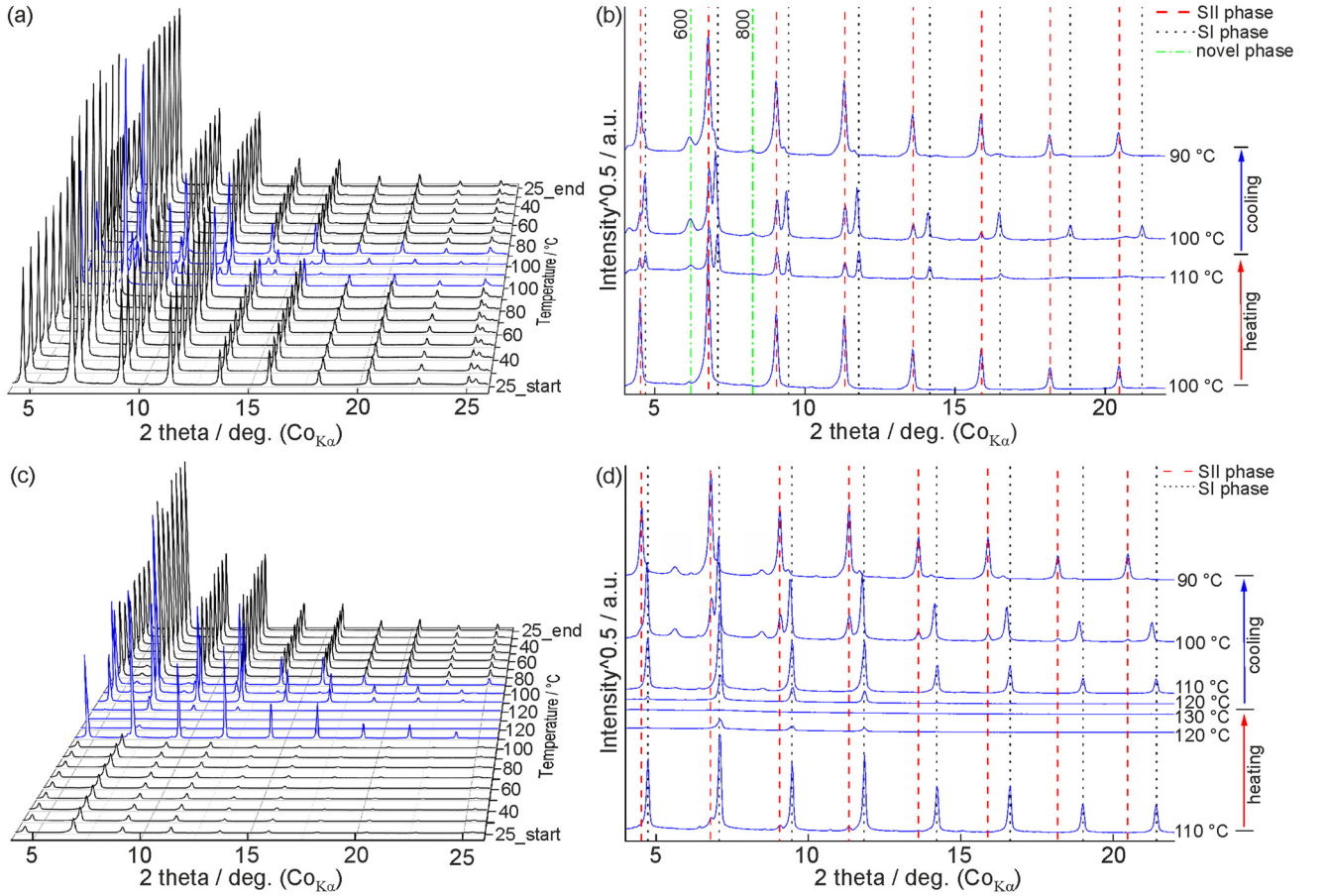

Fig. 2 *In situ* HT-XRPD patterns of Pb(C16)$_2$ + LO_mix (a and b) and powder Pb(C16)$_2$ (c and d). Measurement progression during heating/cooling cycles (a and c) and selected patterns at particular temperatures (b and d). The patterns were collected from 30 °C onwards with an increment of 10 °C (a and c).

initiation is attributed to the presence of linseed oil as also reported by Hermans *et al.*[32] This correlation is supported by our DSC results, which indicate a melting onset at approximately 99 °C (Fig. 1b).

In situ HT-XRPD reveals notable structural changes associated with the transformation of lead palmitate from a crystalline solid phase (SII) to an intermediate (rotator) solid phase (SI). During heating, both pure powder lead palmitate and its mixture with oil (Fig. 2b and d) leads to the formation of the SI phase at 110 °C. This transformation is characterized by the appearance of basal diffraction lines at higher 2θ angles, indicating a reduction of unit cell parameters, primarily along the *a*-axis.[21] Martínez-Casado *et al.* employed pair distribution function (PDF) analysis to investigate these structural changes and revealed a shortening of both Pb–Pb and Pb–O bond distances, which consequently alters the coordination environment of lead atoms.[21]

In the Pb(C16)$_2$ + LO_mix system, *in situ* HT-XRPD pointed to the simultaneous presence of both SII and SI phases at 110 °C (Fig. 2b). This observation reveals that while the phase transformation signals (IL → SI and SI → SII) merged in the DSC endothermic curve of Pb(C16)$_2$ + LO_mix (Fig. 1), the both SII and SI phases remain simultaneously present in the system. Upon cooling down to 100 °C, both phases exhibited increased diffraction intensity, indicating simultaneous growth of the both phase fractions. Further cooling to 90 °C resulted in the persistence of the SII phase only, with SI mesophase having diminished and shifted diffraction signals compared to the pattern at 100 °C (Fig. 2b). These phase transitions correlate closely with the transformation temperatures observed in the DSC analysis at 98.8 °C and 93.7 °C (Fig. 1), which likely correspond to the Pb(C16)$_2$ IL → SI and SI → SII transitions, respectively.

Additional structural changes were observed in the Pb(C16)$_2$ + LO_mix system beginning at 110 °C, marked by the emergence of new 600 and 800 diffraction lines (at 16.57 Å and 12.41 Å, respectively). These signals intensified as the temperature decreased to 100 °C and 90 °C (Fig. 2b). The emergence of these additional diffraction lines aligns with previous DSC observations and suggests the formation of a novel lead carboxylate phase, likely occurring through a dissolution–recrystallization process facilitated by the finite solubility of lead palmitate in linseed oil (approximately 5×10^{-3} mol% at 20 °C, as reported by Hermans *et al.* 2016) and slightly favorable mixing

enthalpy (negative ΔH_{mix}) between metal soap and oil molecules compared to metal soap self-interactions.[32] During the temperature range of 90–80 °C, these maxima exhibited a shift from 16.57 Å to 16.73 Å and 12.41 Å to 12.56 Å, as shown in Fig. S5, ESI.† This peak shift correlates with the phase transformation temperatures observed previously in DSC cooling cycle of the $Pb(C16)_2$ + LO_mix system (Fig. 1 and Table 2). Thus, we can assign the DSC maxima at 102.1 °C and 89.8 °C to the crystallization of SI and SII phase of a neo-formed lead carboxylate, respectively.

Heating of powder $Pb(C16)_2$ to 120 °C resulted in the melting of the SI phase, evidenced by the disappearance of most diffraction peaks, with only minimal residual diffraction lines remaining (Fig. 2d). Further heating to 130 °C induced the formation of the IL phase, characterized by the absence of visible diffraction patterns. During the subsequent cooling, the SI phase recrystallizes at 120 °C and 110 °C, followed by the emergence of the SII phase at 100 °C (Fig. 2d). At this temperature, additional minor diffraction signals were observed (Fig. 2d). These signals progressively diminished throughout the cooling process and were not observed in the final room temperature diffraction pattern (Fig. S6, ESI†). These transient diffraction signals lie close to those of crystalline palmitic acid. However, pure palmitic acid has a melting point around 63 °C and a relatively high solubility in linseed oil,[32] so the appearance of ordered palmitic acid phases at elevated temperatures seems unlikely. A reliable interpretation of these signals remains elusive.

Subsequent *in situ* isothermal HT-XRPD measurement of $Pb(C16)_2$ + LO_mix (Fig. 3a) at 112 °C confirmed the formation of additional crystalline phases. Initially, the sample heated to 112 °C showed no diffraction lines, indicating complete melting of SII to the IL phase. However, after 10 minutes of isothermal heating, distinct diffraction lines emerged and continued to develop throughout the 2-hours measurement period, remaining stable upon cooling to room temperature (Fig. 3a). Quantitative analysis of the integral peak intensities of diffraction patterns recorded between 10 and 110 minutes

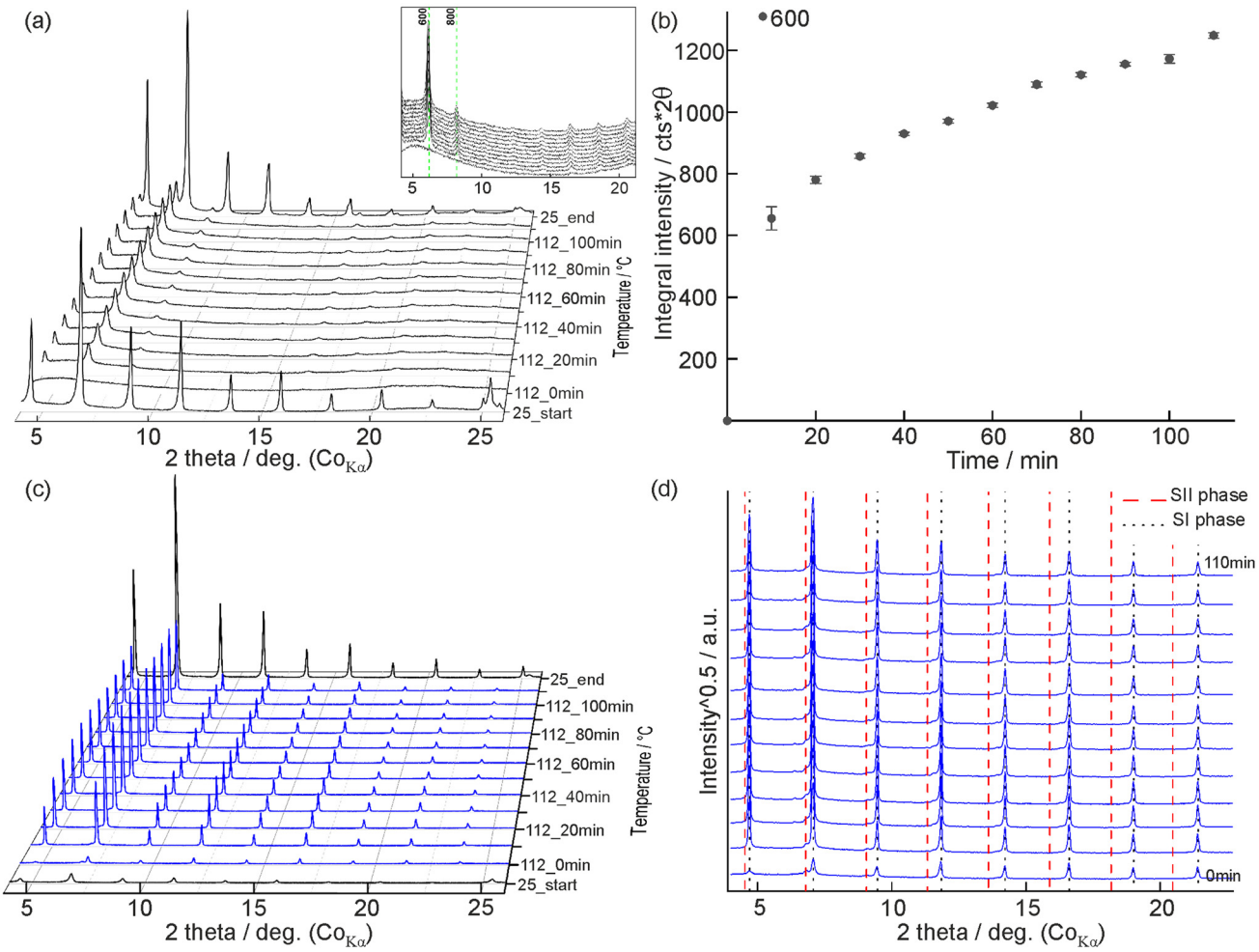

Fig. 3 *In situ* isothermal HT-XRPD patterns of $Pb(C16)_2$ + LO_mix at 112 °C (a); relative integral intensities of the diffraction line 600 attributed to a neo-formed mixed lead carboxylate as a function of time (b); *in situ* isothermal HT-XRPD patterns of powder $Pb(C16)_2$ at 112 °C (c); the comparison of *in situ* isothermal HT-XRPD patterns of powder $Pb(C16)_2$ at 112 °C (c) in a range from 0 to 110 minutes at 112 °C with indicated SII and SI phases (d).

revealed progressive intensity increases of the most intense signals indexed as 600 (16.57 Å) during the isothermal treatment (Fig. 3b). The mixture did not reach equilibrium even after two hours of isothermal heating, suggesting potential for further phase development during extended heating period.

In situ isothermal HT-XRPD measurements of powder lead palmitate at 112 °C (Fig. 3c and d) showed no evidence of additional phase formation, confirming that the presence of linseed oil is essential for this phenomenon. The powder samples exhibited an abrupt increase in diffraction intensity when comparing room temperature diffraction patterns (Fig. 2c and 3c), attributed to material recrystallization with preferred orientation on the platinum heating plate surface in the high-temperature chamber (as described in section 2.3).

The newly formed phase was identified using crystal structures of mixed lead palmitate–stearate compounds (Pb$(C16)_{2-x}(C18)_x$ where x = 0; 0.25; 0.5; 0.75; 1; 1.5; 2) described in our previous research.[30] Analysis of the diffraction pattern obtained after 110 minutes of isothermal heating (Fig. 4a) showed a strong correlation with $Pb(C16)_{0.5}(C18)_{1.5}$, suggesting preferential incorporation of stearate over palmitate components when lead palmitate is heated with linseed oil at 112 °C. To understand the formation mechanism, we considered previous research by Martínez-Casado *et al.*,[21] which demonstrated that $Pb(C16)_2$ in its IL phase maintains local ordering through isolated Pb^{2+}-COO^- units despite disordered alkyl chains. We assume that during the crystallization, free stearic acid from linseed oil interacts with these lead palmitate units to form mixed lead palmitate–stearate complexes. This process appears to be thermodynamically favored due to the higher crystallization temperature of lead stearate, as confirmed by our DSC analysis (Fig. S3(b) and Table S1, ESI†).

Notable irregularities were observed in the basal diffraction line intensities of the newly formed mixed lead palmitate–stearate compared to crystalline lead palmitate. The neo-formed diffraction patterns (Fig. 3a and 4a) exhibit intense low-angle $h00$ lines that rapidly diminish in intensity at higher angles, with minor diffraction signals becoming visible again between 15° and 25° 2θ. Similar diffraction patterns have been previously reported for the liquid crystal phase of lead decanoate at 110 °C, attributed to short-range order[19] and/or zinc soaps of fatty acids containing methyl side-groups on the alkyl chain, which enable the formation of room-temperature liquid crystal structures with low ordering.[51] Furthermore, diffraction patterns suggesting the formation of less ordered undefined long-chain lead carboxylates were reported in model suspensions consisting of lead pigment minium and linseed oil.[52] Based on these comparisons, we propose that the mixed lead soap phase detected during this experiment exhibits lower crystallinity, likely characterized by short-range order around lead atoms and disordered alkyl chains.

To determine the concentration of free stearic acid in the linseed oil, we employed complementary analytical techniques. Total fatty acid composition was quantified using gas chromatography with flame ionization detection (GC-FID), while free fatty acid content was analyzed using ^{1}H and ^{13}C high-resolution nuclear magnetic resonance (HR-NMR) spectroscopy (Fig. S7–S9, ESI†), with detailed methodology provided in ESI.† The results were consistent with previously reported values,[39,53–56] revealing a total free fatty acid (FFA) content of 4.0 (±0.5) mol%. Within this FFA fraction, 12 mol% comprised a mixture of stearic/palmitic acids, which are spectroscopically indistinguishable in the mixture by ^{13}C HR-NMR (Table S2†). Further characterization by GC-FID enabled differentiation of the individual fatty acids, showing that approximately 0.18 mol% consisted of free stearic acid and 0.3 mol% of palmitic acid, based on the characteristic fatty acid composition of linseed oil (Table S3†).

While the formation mechanism remains unknown, literature data on linseed oil degradation at elevated temperatures suggests that our experimental conditions are unlikely to cause significant triacylglycerides hydrolysis resulting in a formation of additional free fatty acids.[55,56] This indicates that the observed phase formation likely relies primarily on the initial free fatty acid content of the oil. To fully understand the extent and kinetics of this reaction, additional experiments with extended exposure times are warranted. Such studies would provide valuable insights into the interactions between lead

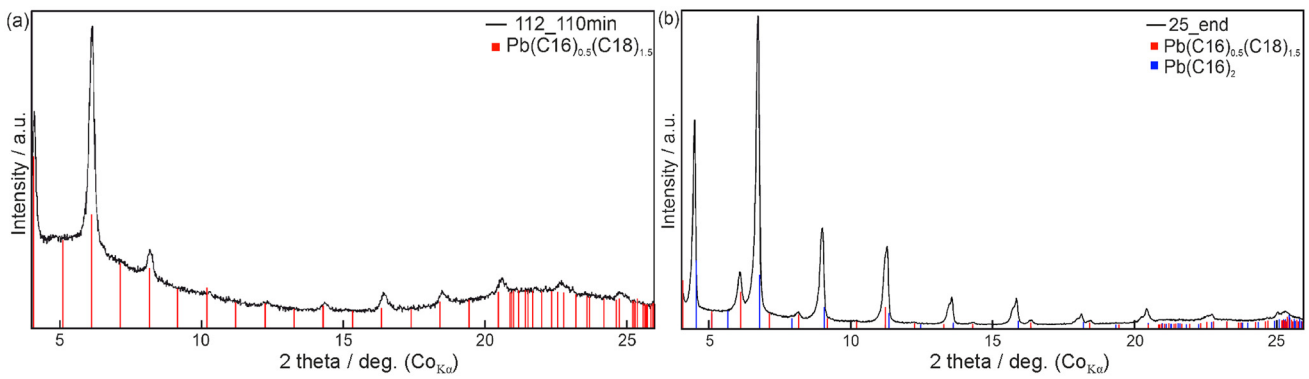

Fig. 4 Phase identification analysis of *in situ* isothermal HT-XRPD of $Pb(C16)_2$ + LO_mix at 112 °C after 110 minutes of isothermal heating (a) and at 25 °C after heating (b).

palmitate and fatty acids, both in their free form and as constituents of triacylglycerides. This could help elucidate whether the limited availability of free stearic acid is a rate-limiting factor in the formation of a mixed lead palmitate–stearate phase.

Room temperature X-ray diffraction analysis of the $Pb(C16)_2$ + LO_mix sample after the isothermal heating (Fig. 4b 25_end) revealed the splitting of diffraction lines associated with the SII phase of lead palmitate into doublets and additional peaks emerging at lower 2θ angles. This pattern indicates the simultaneous formation of a secondary phase alongside the mixed lead carboxylate within the linseed oil matrix.

3.2. Formation of high temperature lead palmitate polymorph in linseed oil

3.2.1 Structural transformations of lead palmitate in linseed oil: insights from XRPD and FTIR analyses. To better understand the nature of the structural changes induced by isothermal heating, we conducted detailed XRPD and FTIR analyses of samples rapidly quenched from 112 °C. *In situ* isothermal HT-XRPD measurements (Fig. 3) revealed intriguing structural changes in lead palmitate mixed with linseed oil when exposed to heat treatment. Considering the relatively rapid heating and cooling rates (approximately 60 °C min^{-1}) during the isothermal measurement program, we conducted an additional experiment involving rapid heating and subsequent quenching of the mixture analogous to $Pb(C16)_2$ + LO_mix sample, as specified in the Experimental section (section 2.1).

The XRPD pattern of the quenched sample ($Pb(C16)_2$ + LO_112 °C) (Fig. 5a) corroborated the findings from the *in situ* isothermal HT-XRPD measurements (section 3.1). We observed the emergence of additional diffraction lines related to the presence of mixed lead palmitate–stearate (400 and 600 lines). Furthermore, we detected a splitting of basal diffraction lines attributed to the lead palmitate SII phase (Fig. 5a).

The observed shift of the split diffraction lines to lower 2θ angles (corresponding to an increase about *ca.* 0.7 Å of *a* parameter) is rather slight in comparison to the diffraction signals of the neo-formed mixed lead carboxylate detected in the system (Fig. 3–5). Assuming a new mixed lead carboxylate could form and taking into account the relationships between *d*-spacing and number of carbons in lead carboxylates reported by Martínez-Casado *et al.*,[21] we would obtain *ca.* 16.08 carbon atoms per a carboxylate group which would correspond to 0.08 mol% of stearate substituting palmitate anions. However, from literature data we can also deduce that such structural change might arise from a polymorphic change of lead palmitate solid phase (SII).[21] Lead *n*-alkanoates can crystallize in two distinct polymorphs: (i) short-chain lead carboxylates typically show a hemi-directed coordination with oxygen atoms positioned on the same side of lead atom (polymorph A, Fig. 6a) and (ii) long-chain lead carboxylates exhibit a holo-directed coordination where oxygen atoms of the carboxylate groups are more symmetrically coordinated around lead atom (polymorph B, Fig. 6b).[24] Within the lead carboxylate series only lead nonanoate and decanoate present both hemi-directed and holo-directed forms at room temperature. While the hemi-directed structures exhibit slightly higher *d*-spacing value and unit cell parameter *a*, the holo-directed forms exhibit higher density.[21] Extrapolating data for *d*-spacing of hemi-directed forms reported by Martínez-Casado *et al.*[21] towards long-chain carboxylates suggests slight increase of *d*-spacing of the most intense diffraction (0.36 Å according to reported relations for both polymorphs) and thus, slight increasing of unit cell parameters, which would result in diffraction lines shifted to lower 2θ angles. Thus, we hypothesize the split diffraction lines could be attributed to the formation of high temperature hemi-directed coordinated polymorph of lead palmitate. To prove this assumption, FTIR spectral features were thoroughly analysed.

The corresponding FTIR spectrum $Pb(C16)_2$ + LO_112 °C (Fig. 5b) revealed several features supporting the formation of

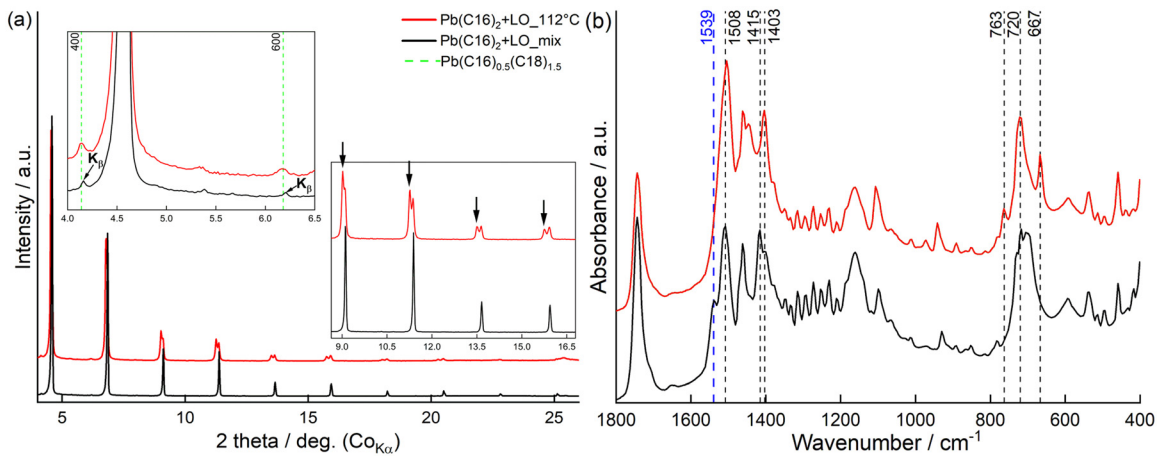

Fig. 5 Comparison of XRPD (a) and FTIR (b) before ($Pb(C16)_2$ + LO_mix, black line) and after ($Pb(C16)_2$ + LO_112 °C, red line) the treatment. XRPD patterns (a) are normalized to specify intensity increase of mixed lead palmitate stearate signals (lines 400 and 600) compared to the K_β lines.

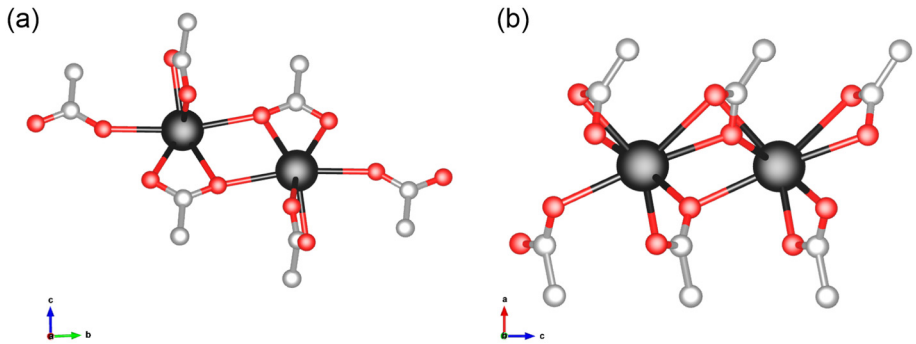

Fig. 6 Two distinct crystalline structures of lead carboxylates: hemi-directed polymorph A (a) and holo-directed polymorph B (b), adapted from Martínez-Casado *et al.*[21] Lead ions are depicted in black, oxygen atoms in red, and carbon atoms in gray. For clarity, only the first two carbon atoms of the alkyl chains adjacent to the carboxylate groups are shown.

a hemi-directed $Pb(C16)_2$ polymorph: (i) absence of a shoulder at 1539 cm^{-1} adjacent to the carboxylate antisymmetric stretching band,[21,28] (ii) shift of the symmetric stretching band from 1415 cm^{-1} to 1403 cm^{-1} and slight shift of the asymmetric one at 1508 cm^{-1}, indicating an altered coordination sphere of the lead atom[24] and (iii) emergence of new spectral signals in the CH_3 rocking vibration area at 763 cm^{-1} and 667 cm^{-1}, accompanied by the merging of bands at 720 cm^{-1} into a single peak.[33,35]

We detected these features also in powder $Pb(C16)_2$ FTIR spectra at 110 °C (SI mesophase) and 120 °C (IL phase), as well as in lead octanoate $Pb(C8)_2$ at room temperature (SII phase). This suggests that the local environment of lead atom in the $Pb(C16)_2$ SI mesophase adopts a coordination similar to the hemi-directed structure in lead octanoate (Fig. 7). This observation corresponds to the assumption of Martínez-Casado *et al.*, deducing from PDF analysis the similarities between the liquid phase (IL) of long-chain lead carboxylates and SII phase of short-chain ones resulting from comparable coordination around the lead atom.[21]

To ensure reproducibility of the obtained results, we conducted an additional experiment to verify the XRPD and FTIR results reported above. The reproduced data and subsequent discussion are provided in the ESI (Fig. S11 and S12, ESI†).

To further validate the hypothesis regarding the formation of a high-temperature hemi-directed $Pb(C16)_2$ polymorph in linseed oil, we performed solid-state nuclear magnetic resonance spectroscopy (ssNMR), providing additional insights into the local structure and bonding environment of lead atoms.

3.2.2 ^{207}Pb ssNMR spectroscopy. The ^{207}Pb ssNMR (^{207}Pb WURST-CPMG NMR and ^{207}Pb spin-echo NMR experiments under static conditions) was used to study the prepared Pb

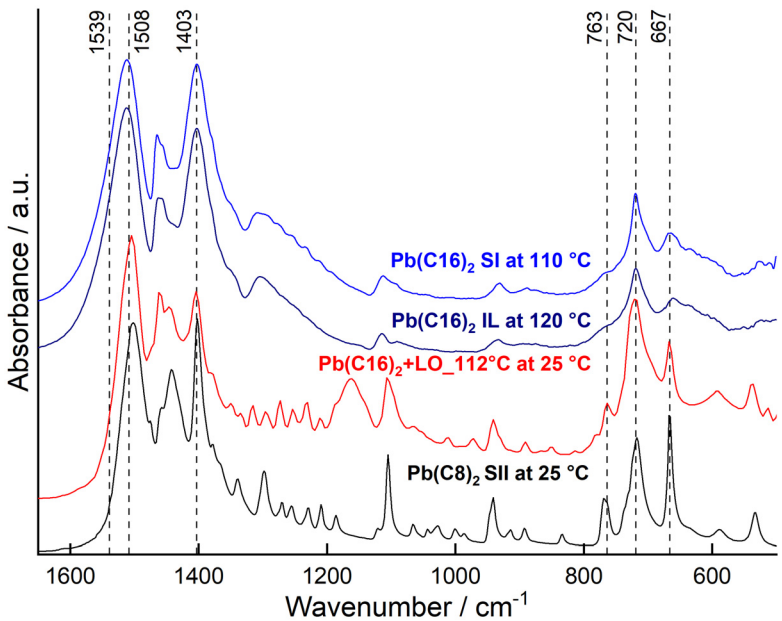

Fig. 7 Comparison of $Pb(C8)_2$ SII phase, $Pb(C16)_2$ SI and IL phases and $Pb(C16)_2$ + LO_112 °C. The spectra of powder $Pb(C16)_2$ cooling from 150 to 35 °C are present in Fig. S10, ESI.†

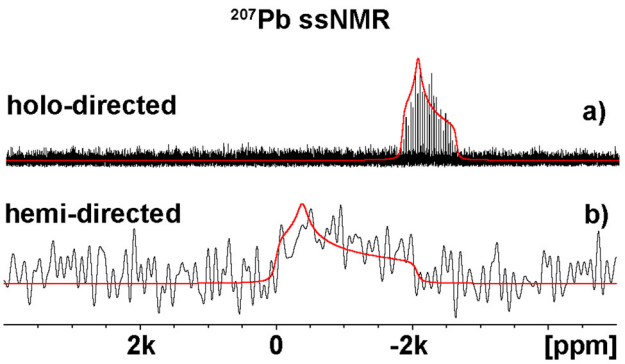

Fig. 8 ^{207}Pb WURST-CPMG NMR (a) and ^{207}Pb spin-echo NMR spectra (b) of investigated $Pb(C16)_2$ + LO_112 °C (black lines) and fitting of the individual lead atoms (red solid lines) in distinct coordination environment. Both ^{207}Pb ssNMR spectra were acquired at temperature 268.2 K.

$(C16)_2$ + LO_112 °C and $Pb(C8)_2$ sample. From Fig. 8 it is suggested that the $Pb(C16)_2$ in LO after the thermal treatment shows a polymorphism similar to the short-chain lead carboxylates.[21] However, the nature of the presented phases requires the use of a different NMR approach. While in the WURST-CPMG NMR experiment (designed for diamagnetic crystalline solids) the $Pb(C16)_2$ crystalline (SII) phase with holo-directed coordination of lead atoms was easily detected, the high-temperature $Pb(C16)_2$ phase having a hemi-directed coordination was undetectable due to the short T_2 relaxation of the lead atoms. One possibility to detect a signal of this high-temperature phase in the ^{207}Pb ssNMR spectrum is offered by the spin-echo NMR experiment (Fig. 8b). Unfortunately, in this case, the signal-to-noise ratio is rather low, and the signal resolution is poor, even when the experiment is performed at a lower temperature (−5 °C) for approximately 6 days. However, the fitting of this signal was carefully done based on known NMR parameters[24] and the experimental ^{207}Pb WURST-CPMG NMR spectrum of lead octanoate (Fig. S13, ESI†). The resulting ^{207}Pb NMR parameters of high-temperature phase of $Pb(C16)_2$ show a significant shift of the detected signal to higher frequencies, which is in good agreement with the trend observed by Catalano *et al.*,[24] for the short-chain lead carboxylates (C6–C8). In addition, the span (breadth) of the signal is slightly lower compared with typical hemi-directed lead carboxylates.[24] This signal narrowing can be explained by the motion of lead atoms in the high-temperature phase, shortening the T_2 relaxation times and at the same time inducing a narrowing of the spectrum. Moreover, the significant discrepancy in ^{207}Pb NMR chemical shift of the hemi-directed polymorph of $Pb(C16)_2$ and model sample $Pb(C8)_2$ may indicate the existence of a mixed hemi-/holo-phase, rather than the formation of two separated domains. The resulting ^{207}Pb ssNMR parameters of the $Pb(C16)_2$ and $Pb(C8)_2$ samples are summarized in Table 3.

It is important to note that upon sufficient exposure to room temperature conditions, the high-temperature hemi-directed phase undergoes transformation to the more thermodynamically stable low-temperature holo-directed phase. As already discussed above, the holo-directed polymorphs exhibit denser packing than the hemi-directed ones. For example, in case of lead nonanoate ($Pb(C9)_2$), the holo-directed polymorph B has density 1.745 g cm^{-3} while density of the hemi-directed polymorph A is 1.718 g cm^{-3}.[21]

Table 3 Experimentally measured ^{207}Pb chemical shift tensor parameters of investigated samples

Sample	Site	δ_{iso} (ppm)	Ω	κ
$Pb(C16)_2$+ LO_112 °C	Holo-	−2155 ± 50	755 ± 50	0.42 ± 0.1
	Hemi-	−283 ± 200	2373 ± 500	0.63 ± 0.3
$Pb(C8)_2$	Hemi-	−1051 ± 50	2768 ± 50	0.63 ± 0.1

The data are presented using the Herzfeld–Berger convention, where $\delta_{iso} = (\delta_{11} + \delta_{22} + \delta_{33})/3$. The span is calculated by $\Omega \approx \delta_{11} - \delta_{33}$ ($\Omega \geq 0$) and the skew is given by $\kappa = 3(\delta_{22} - \delta_{iso})/\Omega$; ($-1 \leq \kappa \leq +1$).[57]

The kinetics of this phase transformation are examined in detail in the subsequent section. Notably, throughout the entire transformation process monitored by XRPD, the characteristic diffraction signals of the mixed lead palmitate–stearate phase persist, remaining clearly resolved in the final diffraction pattern obtained 306 hours after the initiation of the experiment (Fig. S14, ESI†).

3.2.3 Kinetics of high-temperature phase transformation of lead palmitate with linseed oil. The phase transformation kinetics of quenched lead palmitate in linseed oil ($Pb(C16)_2$ + LO_112 °C) was investigated using complementary analytical techniques. XRPD (Fig. 9) and trans-FTIR (Fig. 11) measurements were conducted immediately after quenching and subsequently in regular time intervals to characterize the transformation process.

XRPD patterns collected at 12-hour intervals over 300 hours revealed the progressive isothermal transformation from high-temperature phase (hemi-directed) to low-temperature phase (holo-directed) polymorphs of lead palmitate within the linseed oil matrix (Fig. 9a). Quantitative analysis using BGMN Profex software, fitting the $h00$ ($h = 2n$) diffraction lines with adjusted structural model of lead palmitate,[30] indicated initial phase composition of approximately 60% high-temperature and 40% low-temperature phases (Fig. 9b).

The derivative analysis of the low-temperature phase revealed complex transformation behavior (Fig. 10a and b). While apparent rate fluctuations were observed, these should be interpreted cautiously given the multiple factors that can affect XRPD measurements of such systems, including penetration depth effects and challenges in deconvoluting overlapping reflections from phases with different microstructural characteristics. The transformation, likely proceeding through molecular reorientation of the hemi-directed coordinated polymorph, occurs within the constraining oil matrix, which itself undergoes significant chemical evolution through autoxidative polymerization. While monitored temperature and relative humidity variations within the XRPD chamber showed small deviations that may correlate with the observed rate changes (Fig. S16, ESI†), the complex interplay of multiple experimental

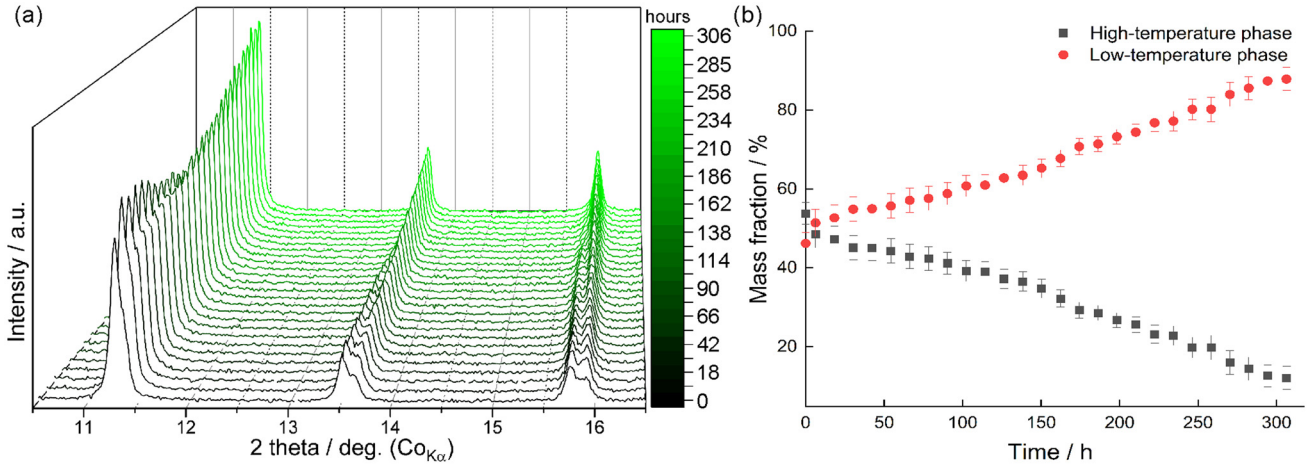

Fig. 9 Progress of transformation in the sample Pb(C16)$_2$ + LO_112 °C followed by XRPD (a) and concentration profiles of both phases (b). Details of fitting are present in Fig. S15 and Table S4, ESI.†

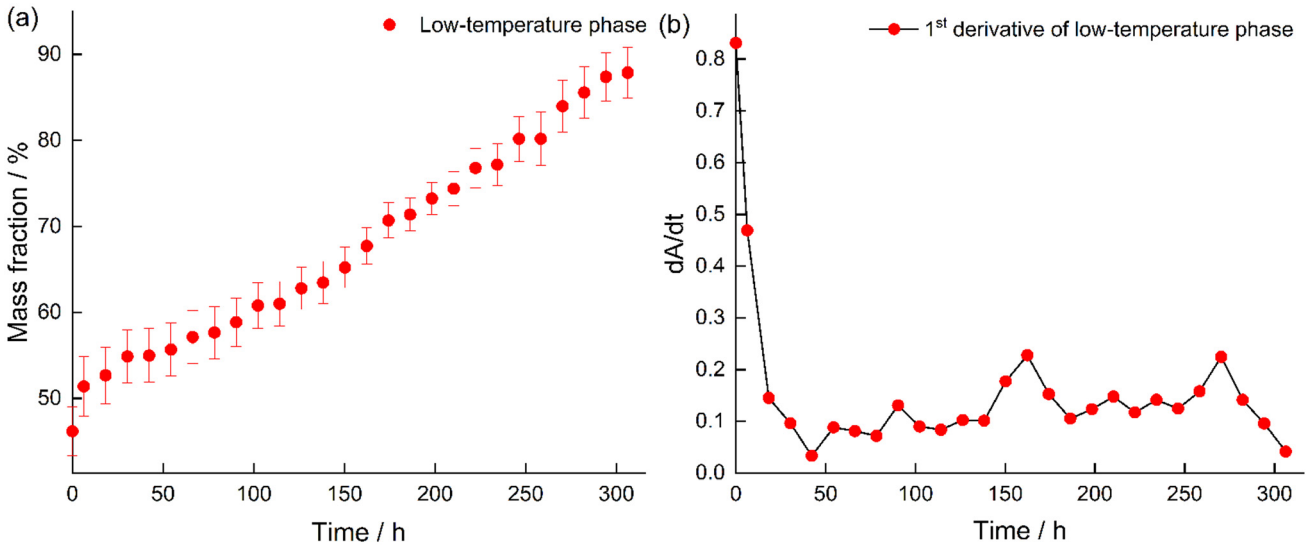

Fig. 10 Concentration–time profile of low-temperature Pb(C16)$_2$ phase in the sample Pb(C16)$_2$ + LO_112 °C (a) and its first derivative (b).

variables makes it difficult to isolate individual contributing factors to the transformation kinetics.

Trans-FTIR spectroscopic analysis conducted over 216 hours (Fig. 11), although not clearly showing the neo-formed bands observed previously (Fig. 5), provided insights into the concurrent linseed oil polymerization process. The intensity of the *cis* C=CH stretching band (3010 cm^{-1}) served as a quantitative measure of polymerization progression, decreasing due to C=C bond oxidation *via* molecular oxygen and/or drier-mediated processes.[36–39,58] Deconvolution analysis of the 3010 cm^{-1} band revealed rapid double bond consumption until 96–120 hours, followed by decreased reaction rates as C=C bonds were depleted (Fig. 11b).

The presence of Pb(C16)$_2$ can significantly influence the oil polymerization kinetics by acting as a drying catalyst. The linseed oil carbonyl region (1800–1650 cm^{-1}) exhibited characteristic changes indicating oxidation product formation, resulting from C=C bond reactions in fatty chains that produce oxygen-containing functional groups such as aldehydes and carboxylic acids (Fig. S18†). As detailed by DePolo *et al.*[39] in their study of linseed oil with PbO pigment as a drier, the carbonyl region showed broadening of the initial signal at 1744 cm^{-1} related to C=O stretching vibration in triglyceride ester groups (υ C=O). This band shifted to 1740 cm^{-1} after 24 hours due to decreased ester concentration and the formation of aldehyde carbonyl stretching bands (υ C=O) and carboxylic acids conjugated to C=C bonds (υ C=O), appearing as bands at 1718 and 1695 cm^{-1}, respectively.[39] These spectral changes correlate with *cis* C=C consumption until bond depletion at 96–120 hours (Fig. 11 and Fig. S18, ESI†).

Research by DePolo *et al.*[39] demonstrated that drier presence accelerates C=C bond consumption until reaching the

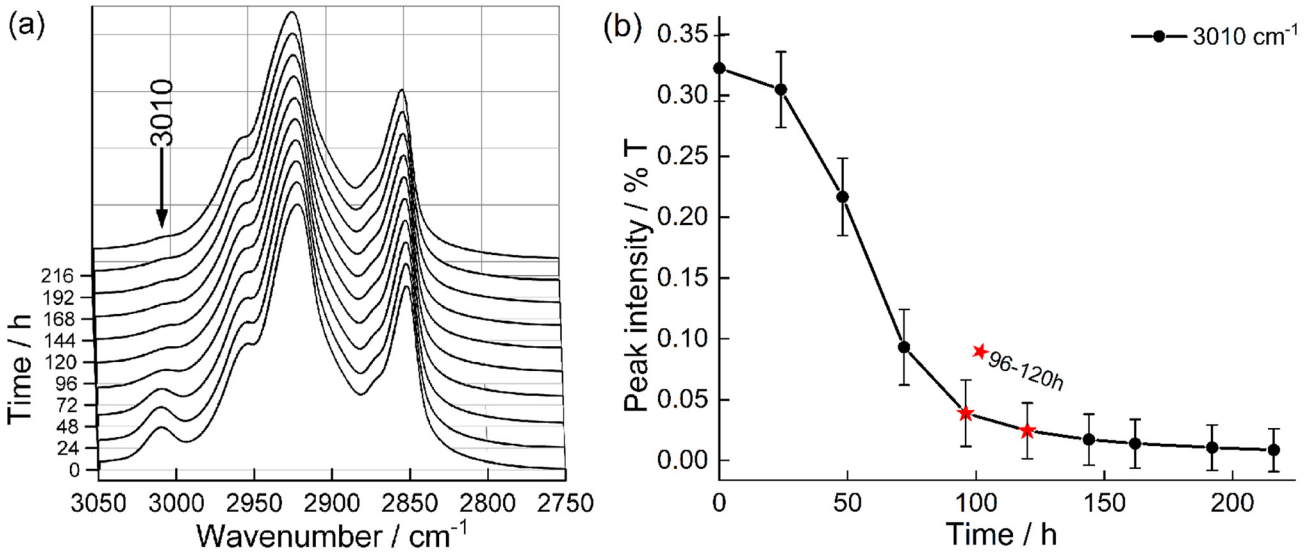

Fig. 11 FTIR spectra of the sample $Pb(C16)_2$ + LO_112 °C normalized to the prominent methylene asymmetric stretching band at 2922 cm^{-1} (a) and intensity change over time of deconvoluted band at 3010 cm^{-1} (b). Deconvolution example is present in ESI (Fig. S17†).

gel point (96–120 hours in this study), after which increased viscosity reduces diffusion of radical initiators and reaction products. The PbO drier induced heterogeneity in cross-link density, significantly impacting overall oil polymerization kinetics. Similarly, $Pb(C16)_2$ in oil preheated to 112 °C likely introduces structural heterogeneity, influencing the lead soap phase transformation kinetics.[39]

The kinetics analysis of lead palmitate transformations demonstrates complex interdependence between the lead palmitate phase transformation and the evolving oil medium. The system behaves as a dynamic composite with concurrent changes in both components potentially generating internal stresses that influence the transformation mechanism and morphology of the product phase. While we made an attempts to fit the data using zero-order kinetics equation (Fig. S19, ESI†), the presence of multiple inflection points in the derivative curves indicates a complex transformation mechanism potentially involving concurrent processes. Further kinetic investigations are warranted to fully elucidate this complex transformation process which is beyond the scope of this publication.

4. Conclusion

This comprehensive investigation of lead palmitate behavior in linseed oil at elevated temperatures has revealed several significant findings with important implications for understanding degradation phenomena in painted artworks such as saponification. First, we demonstrated that heating lead palmitate in linseed oil to 112 °C promotes the formation of mixed lead palmitate–stearate compounds, even with limited free fatty acid availability in the oil medium. This transformation occurs through the preferential incorporation of stearate over palmitate components, suggesting a thermodynamically favored process that may contribute to ongoing degradation in oil paintings. Multiple signals including both simple and mixed lead carboxylate phases visible in DSC exotherm were successfully attributed to the particular phases based on complementing *in situ* HT-XRPD measurements. Specifically, in our system the mixed lead soap close to the composition $Pb(C16)_{0.5}(C18)_{1.5}$ was formed, exhibiting crystallization of SI and SII phase at 102.1 °C and 89.8 °C, respectively.

Second, we identified and characterized a previously unreported high-temperature polymorph of lead palmitate in linseed oil, featuring hemi-directed coordination around lead atoms. This structural arrangement, typically associated with short-chain lead carboxylates, represents a metastable phase that gradually transforms back to the more stable holo-directed configuration under ambient conditions. The transformation process follows complex kinetics with possibly multiple stages, which might be strongly influenced by different factors such as degree of oil polymerization and/or environmental conditions.

These findings have important implications for conservation procedures involving heat treatments, particularly lining techniques. While our study examines transformations at 112 °C, which is higher than the typical lining temperatures of 65–75 °C (ref. 16–18) it demonstrates the potential for complex chemical transformations in lead soap-containing paint layers when exposed to elevated temperatures. The formation of mixed metal soaps and metastable phases suggests that even at lower temperatures, prolonged heat exposure during conservation treatments could potentially initiate subtle chemical changes that continue after treatment. These insights underscore the importance of careful temperature monitoring during lining procedures and considering alternative low-temperature approaches when treating paintings containing

lead-based materials. Further research investigating lead soap behavior at typical lining temperatures would be valuable for developing more targeted conservation protocols.

Furthermore, these findings bring insight into the chemical and structural changes of lead carboxylates arising from their interaction with polymerizing oil medium. While historical paint samples contain more degraded oil with higher proportions of oxygenated groups that could influence reactivity, our observations of complex phase behavior in even relatively simple oil systems help explain the frequent detection of lead soaps with unusual *d*-spacing values or spectral features in authentical paint samples. The formation of mixed metal soaps and metastable phases identified here provides a foundation for understanding crystallization processes in more complex aged oil matrices. Future studies examining these interactions in increasingly realistic paint systems will further bridge the gap between fundamental soap behavior and conservation challenges.

Data availability

Data for this article, including raw data from the XRPD, FTIR, DSC and NMR instruments are available at the digital repository of the Institute of Inorganic Chemistry operated by the Institutional Data Repository of the Czech Academy of Sciences at **https://doi.org/10.57680/asep.0617631**, and alternatively on request at data_repository@iic.cas.cz.

The data supporting this article have been included as part of the ESI.†

Conflicts of interest

There are no conflicts of interest to declare.

Acknowledgements

This work was supported by the Czech Academy of Sciences within the frame of the research programme Strategy AV21 no. 23 – City as a Laboratory of Change: Historical Heritage and Place for Safe and Quality Life. The authors acknowledge the assistance provided by the Research Infrastructure NanoEnviCz, supported by the Ministry of Education, Youth, and Sports of the Czech Republic under project no. LM2023066. A part of the study was performed at the University of Amsterdam during the research stay in the frame of the programme ERASMUS+.

References

1 N. C. Kim and S. H. Song, *Int. J. Polym. Sci.*, 2019, 8094.
2 J. Gao, K. Ye, M. He, W.-W. Xiong, W. Cao, Z. Y. Lee, Y. Wang, T. Wu, F. Huo, X. Liu and Q. Zhang, *J. Solid State Chem.*, 2013, **206**, 27–31.
3 H. Arellano, T. Swebocki, C. Le Coeur, S. Prevost, M. Abdallah, V. Nardello-Rataj and A.-L. Fameau, *J. Colloid Interface Sci.*, 2025, **677**, 314–323.
4 R. A. Weiss, E. Izzo and S. Mandelbaum, *Macromolecules*, 2008, **41**, 2978–2980.
5 A. D. Pomogailo, G. I. Dzhardimalieva and V. N. Kestelman, *Springer Ser. Mater. Sci.*, 2010, **138**, 217–256.
6 S. Mishra, S. Daniele and L. G. Hubert-Pfalzgraf, *Chem. Soc. Rev.*, 2007, **36**, 1770–1787.
7 C. Higgit, M. Spring and D. Saunders, *Natl. Gall. Tech. Bull*, 2003, vol. 24, pp. 75–95.
8 P. Noble, A. van Loon and J. Boon, *ICOM-CC 14th Triennial Meeting, The Hague*, 2005, 496–503.
9 K. Keune and J. J. Boon, *Stud. Conserv.*, 2007, **52**, 161–176.
10 K. Keune, A. Van Loon and J. J. Boon, *Microsc. Microanal.*, 2011, **17**, 696–701.
11 S. Švarcová, E. Kočí, J. Plocek, A. Zhankina, J. Hradilová and P. Bezdička, *J. Cult. Herit.*, 2019, **38**, 8–19.
12 M. Cotte, E. Checroun, W. De Nolf, Y. Taniguchi, L. De Viguerie, M. Burghammer, P. Walter, C. Rivard, M. Salomé, K. Janssens and J. Susini, *Stud. Conserv.*, 2017, **62**, 2–23.
13 E. Ordonez and J. Twilley, *Anal. Chem.*, 1997, **69**(13), 416A–422A.
14 C. S. Tumosa and M. F. Mecklenburg, *Stud. Conserv.*, 2005, **50**, 39–47.
15 J. Rinse, *Am. Paint J.*, 1967, **51**, 22–28.
16 P. Ackroyd, A. Phenix and C. Villers, *Conservation*, 2002, **26**, 14–23.
17 Z. Čermáková, S. Švarcová, J. Hradilová, P. Bezdička, A. Lančok, V. Vašutová, J. Blažek and D. Hradil, *Spectrochim. Acta, Part A*, 2015, **140**, 101–110.
18 S. Hackney, J. Reifsnyder, M. Marvelde and M. Scharff, *Conservation of Easel Paintings*, 2020, vo1. 1, pp. 440–477.
19 F. J. Martínez Casado, M. V. García Pérez, M. I. Redondo Yélamos, J. A. Rodríguez Cheda, A. Sánchez Arenas, S. López-Andrés, J. García-Barriocanal, A. Rivera, C. León and J. Santamaría, *J. Phys. Chem. C*, 2007, **111**, 6826–6831.
20 F. J. Martínez Casado, M. Ramos Riesco, M. I. Redondo Yélamos, A. Sánchez Arenas and J. A. Rodríguez Cheda, *J. Therm. Anal. Calorim.*, 2012, **108**, 399–413.
21 F. J. Martínez-Casado, M. Ramos-Riesco, J. A. Rodríguez-Cheda, M. I. Redondo-Yélamos, L. Garrido, A. Fernández-Martínez, J. García-Barriocanal, I. da Silva, M. Durán-Olivencia and A. Poulain, *Phys. Chem. Chem. Phys.*, 2017, **19**, 17009–17018.
22 F. J. Martínez-Casado, M. Ramos-Riesco, J. A. Rodríguez-Cheda, F. Cucinotta, A. Fernández-Martínez, L. Garrido, E. Matesanz and L. Marchese, *J. Mater. Chem. C*, 2014, **2**, 9489–9496.
23 F. J. Martínez Casado, M. Ramos Riesco, A. Sánchez Arenas, M. V. García Pérez, M. I. Redondo, S. López-Andrés, L. Garrido and J. A. R. Cheda, *J. Phys. Chem. B*, 2008, **112**, 16601–16609.
24 J. Catalano, A. Murphy, Y. Yao, G. P. A. Yap, N. Zumbulyadis, S. A. Centeno and C. Dybowski, *Dalton Trans.*, 2014, **44**, 2340–2347.

25 J. Catalano, V. Di Tullio, M. Wagner, N. Zumbulyadis, S. A. Centeno and C. Dybowski, *Magn. Reson. Chem.*, 2020, **58**, 798–811.
26 H. A. Ellis, N. A. S. White, R. A. Taylor and P. T. Maragh, *J. Mol. Struct.*, 2005, **738**, 205–210.
27 M. S. Akanni and N. A. Abass, *Liq. Cryst.*, 1989, **6**(5), 597–608.
28 M. S. Akanni, H. D. Burrows, H. A. Ellis, D. N. Asongwed, H. B. Babalola and P. O. Ojo, *J. Chem. Technol. Biotechnol., Chem. Technol.*, 1984, **34A**, 127–135.
29 M. S. Akanni, E. K. Okoh, H. D. Burrows and H. A. Ellis, *Thermochim. Acta*, 1992, **208**, 1–41.
30 E. Kočí, J. Rohlíček, L. Kobera, J. Plocek, S. Švarcová and P. Bezdička, *Dalton Trans.*, 2019, **48**, 12531–12540.
31 J. J. Hermans, K. Keune, A. van Loon, M. J. N. Stols-Witlox, R. W. Corkery and P. D. Iedema, *ICOM-CC 17th Trienn. Conf. Prepr. Melb.*, 2014, preprint 1603.
32 J. J. Hermans, K. Keune, A. Van Loon and P. D. Iedema, *Phys. Chem. Chem. Phys.*, 2016, **18**, 10896–10905.
33 H. A. Ellis, *Mol. Cryst. Liq. Cryst.*, 1986, **139**, 281–290.
34 M. A. Mesubi, *J. Mol. Struct.*, 1982, **81**, 61–71.
35 J. Hermans, L. Zuidgeest, P. Iedema, S. Woutersen and K. Keune, *Phys. Chem. Chem. Phys.*, 2021, **23**, 22589–22600.
36 J. van der Weerd, A. van Loon and J. J. Boon, *Stud. Conserv.*, 2005, **50**, 3–22.
37 R. J. Meilunas, J. G. Bentsen and A. Steinberg, *Stud. Conserv.*, 1990, **35**, 33–51.
38 L. de Viguerie, P. A. Payard, E. Portero, Ph. Walter and M. Cotte, *Prog. Org. Coat.*, 2016, **93**, 46–60.
39 G. DePolo, P. Iedema, K. Shull and J. Hermans, *Macromolecules*, 2024, **57**, 8263–8276.
40 T. Degen, M. Sadki, E. Bron, U. König and G. Nénert, in *Powder Diffraction*, Cambridge University Press, 2014, vol. 29, 13-S18.
41 PDF-5+ database, release 2025 International Centre for Diffraction Data, Newtown Square, PA. U.S.A., 2024.
42 H. M. Rietveld, *J. Appl. Crystallogr.*, 1969, **2**, 65–71.
43 J. Bergmann, P. Friedel and R. Kleeberg, CPD Newsletter (Commission of Powder Diffraction, International Union of Crystallography), 1998, **20**, 5–8.
44 J. Bergmann, T. Monecke and R. Kleeberg, *J. Appl. Crystallogr.*, 2001, **34**, 16–19.
45 N. Döbelin and R. Kleeberg, *J. Appl. Crystallogr.*, 2015, **48**, 1573–1580, DOI: **10.1107/S1600576715014685**.
46 T. Degen and T. Dortmann, HighScorePlus, version 5.3.0.33005, October 1, 2024, XHP_CHMPrint.pdf file, page 421.
47 L. A. O'Dell and R. W. Schurko, *Chem. Phys. Lett.*, 2008, **464**, 97–102.
48 J. Tang, L. O'Dell, P. Aguiar, B. Lucier, D. Sakellariou and R. Schurko, *Chem. Phys. Lett.*, 2008, **466**, 227–234.
49 E. L. Hahn, *Phys. Rev.*, 1950, **80**, 580–594.
50 J. Brus, *Solid State Nucl. Magn. Reson.*, 2000, **16**, 151–160.
51 R. W. Corkery, *Phys. Chem. Chem. Phys.*, 2004, **6**, 1534–1546.
52 S. Švarcová, E. Kočí, P. Bezdička, S. Garrappa, L. Kobera, J. Plocek, J. Brus, M. Šťastný and D. Hradil, *Dalton Trans.*, 2020, **49**, 5044–5054.
53 V.-M. Popa, A. Gruia, D. N. Raba, D. Dumbrava, C. Moldovan, D. Bordean and C. Mateescu, *J. Agroaliment. Processes Technol.*, 2012, **18**(2), 136–140.
54 Y. El-Shattory, *Food/Nahrung*, 1976, **20**, 307–311.
55 M. Lazzari and O. Chiantore, *Polym. Degrad. Stab.*, 1999, **65**, 303–313.
56 B. M. Berto, R. K. A. Garcia, G. D. Fernandes, D. Barrera-Arellano and G. G. Pereira, *Grasas Aceites*, 2020, **71**(1), e337.
57 J. Herzfeld and A. E. Berger, *J. Chem. Phys.*, 1980, **73**, 6021–6030.
58 J. Mallégol, J. Lemaire and J.-L. Gardette, *Prog. Org. Coat.*, 2000, **39**, 107–113.